Conference on Modelling Fluid Flow (CMFF'22)
The 18th International Conference on Fluid Flow Technologies
Budapest, Hungary, August 30-September 2, 2022

EXPANSION AND COLLAPSE OF SINGLE CAVITATION BUBBLES RIGHT AT A SOLID BOUNDARY

Christiane LECHNER[1], Max KOCH[2], Werner LAUTERBORN[2], Robert METTIN[2],

[1] Corresponding Author. Institute of Fluid Mechanics and Heat Transfer, TU Wien. Getreidemarkt 9, A-1060 Vienna, Austria. Tel.: +43 1 58801 32211, Fax: +43 1 58801 32298, E-mail: christiane.lechner@tuwien.ac.at
[2] Third Physical Institute, Georg-August University Göttingen. Germany. E-mail: max.koch@phys.uni-goettingen.de, werner.lauterborn@phys.uni-goettingen.de, robert.mettin@phys.uni-goettingen.de

ABSTRACT

We present results from numerical simulations modeling the dynamics of single (laser-generated) cavitation bubbles expanding and collapsing right at a plane solid boundary. The model consists of a bubble filled with a small amount of non-condensable gas in a compressible liquid. The Navier-Stokes equations are discretized with the finite volume method. The volume of fluid method is used to capture the interface between liquid and gas. The model is implemented in the open source software package OpenFOAM.

A millimeter sized bubble in water serves as reference to discuss bubble dynamics. The most intriguing phenomenon that occurs in this configuration is the formation of a fast jet that is directed towards the solid with a speed of the order of 1000 m/s. The jet formation mechanism is explained. Paradoxically, in this setting, jet formation causally is related to the viscosity of the liquid.

Bubble size and liquid viscosity are varied. It is shown that fast jet formation persists for a wide range of liquid viscosities, including e.g. 50 cSt silicone oil. Bubble dynamics and the jet formation mechanism are discussed for values of a bubble Reynolds number, Re_b, ranging from 15 to 50 000, with fast jet formation occurring for $\mathrm{Re}_b \gtrsim 300$.

Keywords: bubble dynamics, cavitation, erosion, finite volume method, jet formation

NOMENCLATURE

B	$[Pa]$	Tait pressure
n_T	$[-]$	Tait exponent
p	$[Pa]$	pressure
t	$[s]$	time
x, y, z	$[\mu m]$	coordinates
$\boldsymbol{U}$	$[m/s]$	velocity
$\mathbb{T}$	$[kg/(ms^2)]$	viscous stress tensor
$\mathcal{R}^{\mathrm{eq}}$	$[\mu m]$	equivalent bubble radius
γ_g	$[--]$	adiabatic exponent, gas
μ	$[kg/(ms)]$	dynamic viscosity
ν	$[m^2/s]$	kinematic viscosity
ρ	$[kg/m^3]$	density
σ	$[kg/s^2]$	surface tension coefficient

Subscripts and Superscripts

init	initial conditions
jet, jf	jet, jet formation
l, g	liquid, gas
max	maximum
∞	ambient conditions

1. INTRODUCTION

Due to their erosive power, cavitation bubbles collapsing close to solid boundaries have been subject to intense investigations for several decades. Mainly two phenomena associated with the collapse of the bubble are considered responsible for the destructive action: a high-speed, axial liquid jet directed towards the solid and the shock waves emitted after the collapse of the resulting torus bubble.

Usually, jets form by involution of the bubble wall and reach a speed of the order of 100 m/s under normal ambient conditions [1, 2, 3, 4], see also [5, Fig. 21]. For bubbles expanding and collapsing in ultimate proximity to the solid, however, very thin axial jets of the order of 1000 m/s are formed, following the violent self-impact of annular liquid inflow at the axis of symmetry [6, 7, 4, 8, 9] and [10].

The mechanism of fast jet formation as well as the explanation of the typical "bell shape" of the bubble during collapse, that is observed in the experiment, see Figure 1, is briefly sketched in Figures 2 – 4 for a millimeter sized bubble in water. Shown are the bubble shape together with the velocity or pressure field at several stages of bubble evolution. During the rapid expansion of the bubble a boundary layer adjacent to the solid forms, as indicated in Fig. 2 (top). This boundary layer causes the outer rim of the bubble to slightly "lift-off" from

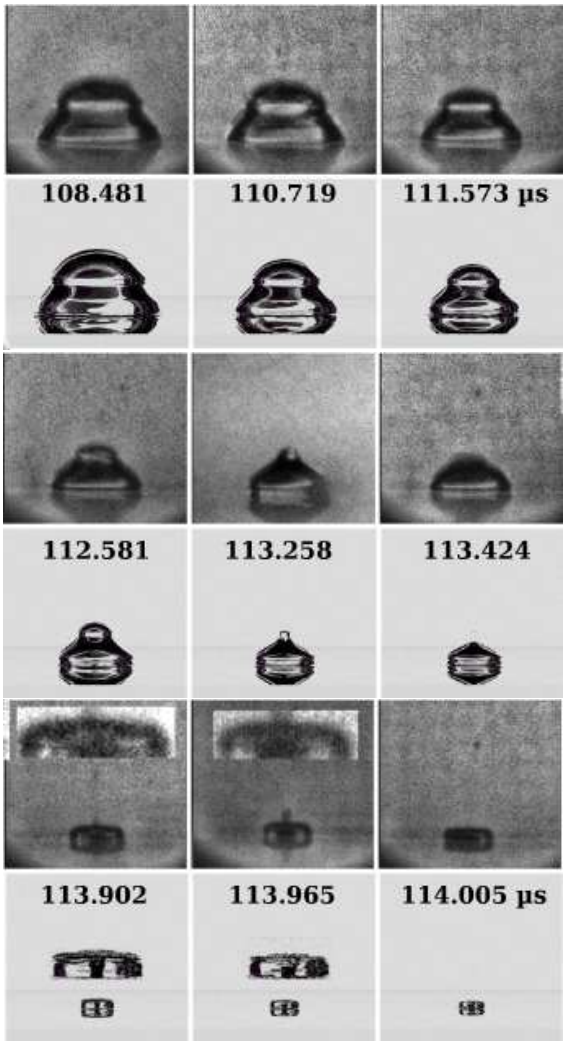

Figure 1. Bubble collapsing right at a plane solid boundary in water, taken from [9, Fig. 16]. Comparison of experimental high-speed photographs (odd rows) and the result of ray-tracing a numerical 3D simulation (even rows). In the last two rows magnifications with enhanced contrast are shown as inserts. Frame width 664.5 μm.

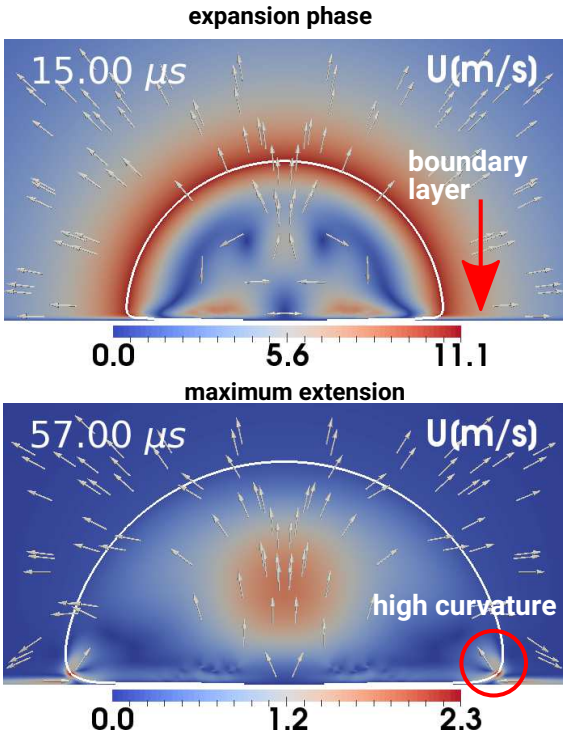

Figure 2. Bubble expanding right at a plane solid boundary in water. Results of an axially symmetric simulation. Shown is a cut through the bubble. The color gives the magnitude of the velocity in m/s. Arrows indicate the direction of the flow. At $t = 57\mu s$ the bubble attains the maximum volume with $\mathcal{R}^{eq}_{max} = 627\mu m$. Frame size 1.6 × 0.8 mm.

the solid surface. At maximum extension the bubble shape is hemi-spherical, except for the region around the outer bubble rim, which exhibits a much larger curvature than the remainder of the bubble, see Fig. 2 (bottom). For bubbles in a low viscosity liquid, such as water, this deviation from hemi-spherical shape might seem marginal. Nevertheless, it is decisive for the fast jet forming in the late collapse phase. The high curvature region at the outer rim collapses faster than the remainder of the bubble leading to an indentation, as shown in Figs 1 and 3.

The indentation sharpens and leads to an annular inflow, that arrives faster at the axis of symmetry, than the spherical cap comes down. As a result, the annular inflow impacts onto itself, momentarily generating a very high pressure. The self-impact leads to the emission of a shock wave and liquid is squeezed into the bubble in form of a very fast, thin jet, see Fig. 4 (middle). The jet ist also seen in the experimental photograph in Fig. 1 in the last but one row. Subsequently, the jet impacts onto the solid with a speed of the order of 1000 m/s, causing a large pressure load on the solid. Finally, the remaining torus bubble collapses, accompanied by the emission of a torus shock wave, see Fig. 4 (bottom).

First photographs of this type of fast jet have been given in [11] for a bubble under reduced ambient pressure, however, no interpretation could be given then. Photographic evidence of the fast jet under normal ambient conditions could only be given recently in [8, 9]. With a combination of experimental photographs and ray-tracing a 3D numerical simulation, see Fig. 1, a lower bound of $732 m/s$ was estimated for the average speed of the fast jet. Recently, [10] presented new experimental evidence for the fast jet, including photographic recordings of the shock wave that is emitted after self-impact of the annular inflow, see Fig. 4. A lower bound of $850 m/s$ for the average jet speed could be inferred from these photographs.

Since the fast annular inflow causally is related to the viscosity of the liquid, it is of interest to quantify the influence of liquid viscosity on the jet formation process. Considering, that in low viscos-

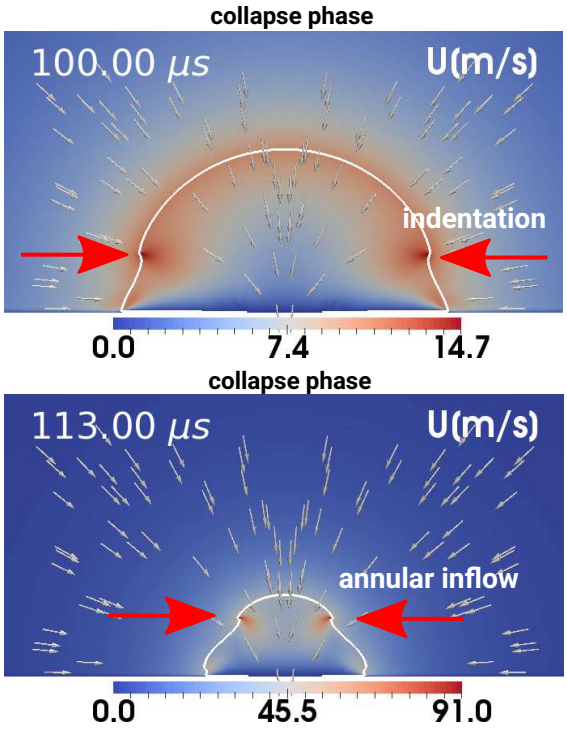

Figure 3. Collapse phase of the bubble in Figure 2. The color gives the magnitude of the velocity in m/s. Frame size 1.6 × 0.8 mm.

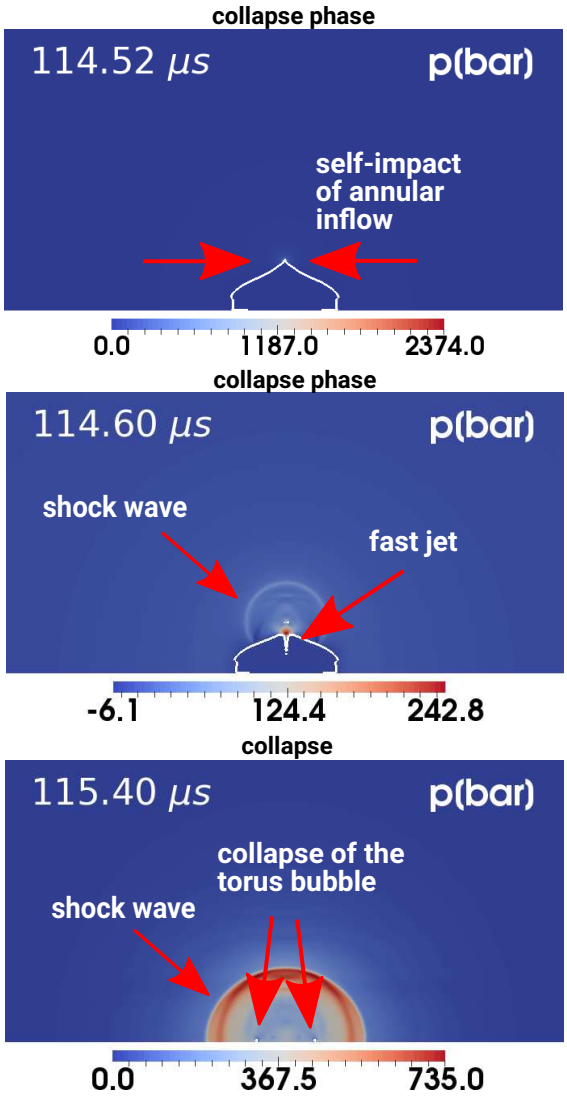

Figure 4. Fast jet formation and final stages of the collapse of the bubble in Figure 2. The color gives the pressure in bar. Frame size 1.6 × 0.8 mm.

ity liquids the bubble shape at maximum extension is hemi-spherical to a very good extent, the equivalent radius of a hemi-sphere,

$$\mathcal{R}^{\rm eq}_{\rm max} := (3V_{\rm max}/(2\pi))^{1/3}, \qquad (1)$$

with $V_{\rm max}$ the maximum volume of the bubble, is taken as a measure of bubble size. Given this, it is natural to define a dimensionless number, a bubble Reynolds number Re_b, from $\mathcal{R}^{\rm eq}_{\rm max}$, the velocity scale $\sqrt{p_\infty/\rho_{l,\infty}}$, and the kinematic viscosity of the liquid, $\nu_l = \mu_l/\rho_{l,\infty}$, as

$$\mathrm{Re}_b = \frac{\mathcal{R}^{\rm eq}_{\rm max}\sqrt{p_\infty/\rho_{l,\infty}}}{\nu_l}, \qquad (2)$$

where p_∞ is the ambient pressure and $\rho_{l,\infty}$ denotes the density of the liquid at ambient conditions.

Bubbles expanding and collapsing right at a solid boundary in liquids with different viscosities have been investigated experimentally by [12] and [13] in different contexts. In [12] the ejection of liquid through a hole in the plate was investigated, whereas the investigations in [13] were in view of laser ablation in liquids. Both works did not investigate the mechanisms of jet formation.

In the following, we vary two parameters, bubble size and viscosity of the liquid, and numerically study the overall dynamics of the bubbles as well as the formation of jets. The bubble shown in Figs 2 – 4 serves as reference for the parameter study. The Reynolds number of the reference bubble with $\mathcal{R}^{\rm eq}_{\rm max} = 627\mu m$ under normal ambient conditions in water evaluates to $\mathrm{Re}_b = 6289$.

We present the bubble model and the numerical implementation in Section 2. Results from the parameter studies are presented in Section 3 and Conclusions are given in Section 4.

2. BUBBLE MODEL AND NUMERICAL IMPLEMENTATION

The bubble model consists of a bubble filled with a small amount of non-condensable gas (air) surrounded by a liquid. The gas is taken to be ideal, undergoing adiabatic changes of state, $p\rho_g^{-\gamma_g} = \text{const}$, with p the pressure, ρ_g the density of the gas and γ_g the ratio of specific heats ($\gamma_g = 1.4$ for air). Phase transition is not considered here. The liquid is modeled as a compressible fluid with the Tait equation of state, $(p + B)\rho_l^{-n_T} = \text{const}$, with ρ_l the density of the liquid, B the Tait pressure and n_T the Tait exponent, taken to be $B = 305MPa, n_T = 7.15$ here. The vapor pressure is small compared to the ambient pressure of

$p_\infty = 101315$ Pa and therefore is neglected. Thermodynamic effects, mass exchange through the bubble wall as well as gravity are neglected. Liquid and gas are considered as viscous fluids. In particular, including the viscosity of the liquid is essential for fast jet formation here. Surface tension is included, but is not essential for the findings presented here.

The equations are formulated for a single fluid with density ρ, pressure p and velocity $\boldsymbol{U}$ satisfying the Navier-Stokes equation (3) and continuity equation (4). In order to distinguish between the two phases liquid and gas, volume fractions α_l and α_g are introduced, with $\alpha_l = 1$ in the liquid phase and $\alpha_l = 0$ in the gas phase and $\alpha_g = 1-\alpha_l$. Since no mass transfer across the interface is considered, the individual phases satisfy the continuity equations (5).

$$\frac{\partial(\rho\,\boldsymbol{U})}{\partial t} + \boldsymbol{\nabla}\cdot(\rho\,\boldsymbol{U}\otimes\boldsymbol{U}) = -\boldsymbol{\nabla}p + \boldsymbol{\nabla}\cdot\mathbb{T} + \boldsymbol{f}_\sigma\,, \quad (3)$$

$$\frac{\partial\rho}{\partial t} + \boldsymbol{\nabla}\cdot(\rho\,\boldsymbol{U}) = 0\,, \quad (4)$$

$$\frac{\partial(\alpha_i\rho_i)}{\partial t} + \boldsymbol{\nabla}\cdot(\alpha_i\rho_i\boldsymbol{U}) = 0\,, \qquad i = l, g\,. \quad (5)$$

$\boldsymbol{\nabla}$ denotes the gradient, $\boldsymbol{\nabla}\cdot$ is the divergence, and $\otimes$ the tensorial product. The density field, ρ, is written as $\rho = \alpha_l\rho_l + \alpha_g\rho_g$. $\mathbb{T}$ is the viscous stress tensor of a Newtonian fluid,

$$\mathbb{T} = \mu\left(\boldsymbol{\nabla}\boldsymbol{U} + (\boldsymbol{\nabla}\boldsymbol{U})^T - \frac{2}{3}(\boldsymbol{\nabla}\cdot\boldsymbol{U})\,\mathbb{I}\right), \quad (6)$$

with $\mu = \alpha_l\mu_l + \alpha_g\mu_g$, where μ_l, μ_g are the dynamic viscosities of liquid and gas, taken to be constant here. Surface tension is included via a force density field $\boldsymbol{f}_\sigma(\boldsymbol{x}, t)$ [see, e.g., 14].

Equations (3)–(5) are discretized with the finite volume method. The numerical implementation is based on the open source software package OpenFOAM [15, 16]. A pressure based two-phase solver is adapted for our purpose [17].

Simulations are performed in axial symmetry. A sketch of the computational domain and the grid structure is given in Figure 5. The grid is Cartesian with a uniform grid spacing of $\Delta x \approx \mathcal{R}^{\mathrm{eq}}_{\mathrm{max}}/627$ in an inner region. Further out, a polar cell ordering is used with the grid spacing increasing progressively in radial direction. The number of cells typically amounts to 140 000 for this series of runs.

Initially, a small hemi-spherical bubble with radius $\mathcal{R}_{\mathrm{init}}$ and high internal pressure $p_{\mathrm{g,init}} \gg p_\infty$ is placed in the still liquid directly at the solid surface. p_∞ denotes the ambient pressure, which is set to $p_\infty = 101315Pa$ in all simulations.

At the solid surface no-slip boundary conditions are imposed for the velocity, $\boldsymbol{U} = 0$, the normal derivative of pressure is set to zero, $\partial_n p = 0$, and the liquid volume fraction α_l is set to 1 at the solid. At the outer boundary approximate non-reflecting boundary conditions are specified for velocity and pressure.

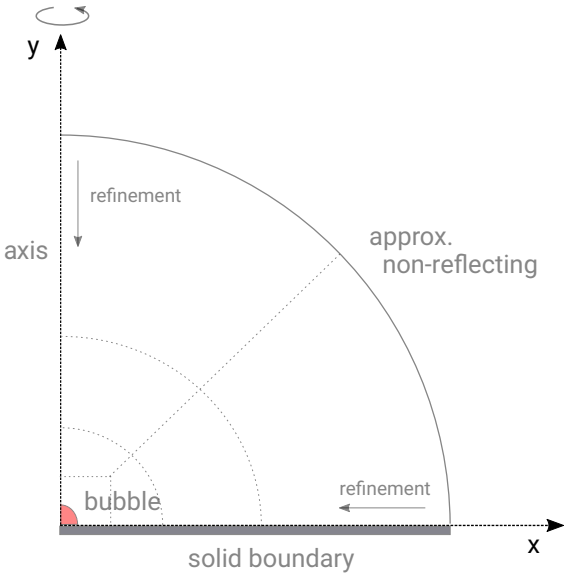

Figure 5. Sketch of the computational domain and the grid structure (not to scale).

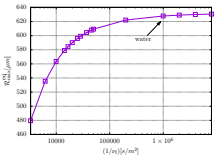

Figure 6. Maximum radius of the bubble as a function of $1/\nu_l$ for series 1. The reference bubble is indicated by an arrow.

3. RESULTS

Bubble dynamics is investigated by means of several series of simulations. Essentially, two parameters are varied, the bubble size and the viscosity of the liquid. In this investigation Re_b varies from 16 to 50 600. Four one-parameter series of simulations are presented.

In **series 1** the liquid viscosity is varied between $\mu_l = 0.125\mu_{H_2O}$ and $\mu_l = 300\mu_{H_2O}$, while initial data $\mathcal{R}_{\mathrm{init}} = 2^{1/2}20\mu m$, $p_{\mathrm{g,init}} = 1.1 \times 10^4 bar$ are kept fixed. The reference bubble is included in this series. The bubble Reynolds numbers lie in the interval $\mathrm{Re}_b \in [16, 50605]$. Figure 6 shows the maximum equivalent radius as a function of $1/\nu_l$. As expected, the maximum radius decreases with increasing viscosity, as the portion of the bubble energy that is dissipated increases.

For **series 2–4** the liquid properties are kept fixed and the maximum radius of the bubble is varied by changing initial data. The three liquids under con-

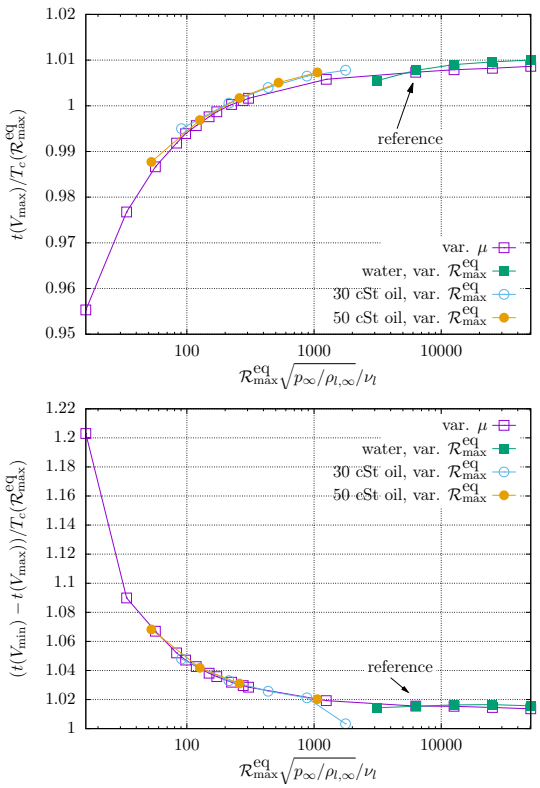

Figure 7. Time from bubble inception to the maximum extension (top) and time from the maximum extension to the first collapse (bottom).

sideration are water and 30 cSt and 50 cSt silicone oils. Material properties of the 30 cSt silicone oil are $\rho_{l,\infty} = 971\,kg/m^3, \mu_l = 0.029\,kg/(ms)$ yielding $\nu_l = 29.9\times10^{-6} m^2/s$ and of the 50 cSt silicone oil $\rho_{l,\infty} = 956\,kg/m^3, \mu_l = 0.0478\,kg/(ms), \nu_l = 50\times10^{-6}\,m^2/s$. For water $\rho_{l,\infty} = 998.2 kg/m^3$ $\mu_l = 0.0001 kg/(ms)$. The reference bubble is included in series 2. Overall, the maximum radii $\mathcal{R}^{eq}_{max}$ vary between 255 μm and 5200 μm. The bubble Reynolds numbers span the range between 52 and 50500.

Figure 7 shows the time from the initial conditions to the maximum extension, $t(V_{max})$, normalized with the Rayleigh collapse time, $T_c(\mathcal{R}^{eq}_{max}) = 0.915\,\mathcal{R}^{eq}_{max}\sqrt{\rho_{l,\infty}/p_\infty}$, of a bubble with radius $\mathcal{R}^{eq}_{max}$ (top). For low viscosity liquids this ratio is close to 1. With increasing viscosity or decreasing bubble size this quantity slightly decreases. The time from maximum extension to the first collapse, on the other hand, considerably decreases with increasing viscosity or decreasing bubble size, as shown in Fig. 7 (bottom). In total, expansion and collapse get more and more asymmetric with increasing viscosity or decreasing bubble size.

Figure 8 shows the bubble shape at maximum extension for selected values of the bubble Reynolds number including the reference bubble with $\mathrm{Re}_b = 6289$. The thickness of the viscous boundary layer during the expansion phase increases with decreasing bubble Reynolds number. As a consequence the dis-

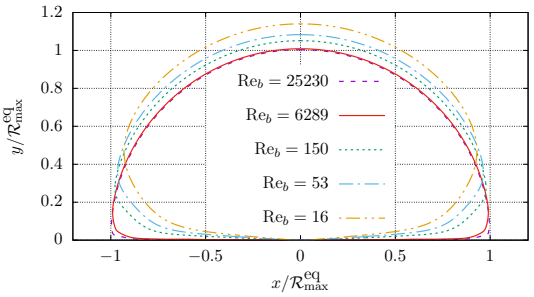

Figure 8. Bubble shapes at maximum extension for different values of Re_b taken from series 1,2 and 4. The solid line represents the reference bubble (water, $\mathcal{R}^{eq}_{max} = 627\mu m$, $\mathrm{Re}_b = 6289$)

tance of the outer rim of the bubble at maximum extension increases with decreasing Re_b. Furthermore, with decreasing Reynolds number bubble expansion along the solid wall is hindered and expansion in the direction orthogonal to the solid is increased. In total, the bubble shape changes from hemi-spherical with a slight "elevation" of the outer bubble rim for very high Reynolds numbers to a shape that resembles more an oblate spheroid for small Reynolds numbers.

Figure 9 shows the bubble shapes during collapse for four liquids from series 1, including the reference bubble. In water with $\mathrm{Re}_b = 6289$ the high curvature region at the outer bubble rim involutes and the bubble shape shows the indentation that has been described in Sec. 1. The indentation ultimately leads to the self impact of the annular inflow and the formation of the fast jet. For $\mathrm{Re}_b = 150$ (second row) the higher curvature region at the outer bubble rim involutes as well. However, here the higher viscosity damps the relative motion and no annular inflow, faster than the surroundings, develops. The bubble surface stays smooth. The timing is such, that a spherical cap with higher curvature on top of the bubble is developing, which collapses faster than the bubble sides. A jet forms at the end of the collapse of the spherical cap by involution of the bubble wall. The speed of the jet for this value of Re_b amounts to approximately 500 m/s.

For even smaller Reynolds numbers $\mathrm{Re}_b = 34$ and 16 (Fig. 9 third and last row), there seem to be three regions during bubble collapse. A region close to the solid, where there is hardly any movement, a middle region around the "belly" of the bubble, which collapses faster and involutes, and a cap which seems to collapse in an approximately spherical manner. These three regions are indicated and separated by sharp edges in the bubble shape, which are more pronounced for the smaller Reynolds number. We note, that these sharp edges are not a numerical artefact, but are seen in the experiment as well, compare e.g. the shape of a collapsing bubble in PAO40 in

[13]. A broad jet with a speed of 110 m/s is formed by involution of the bubble wall for $\mathrm{Re}_b = 34$. There is no jet formation for $\mathrm{Re}_b = 16$.

Figures 10 and 11 show the bubble shape and pressure field around jet formation for the bubbles with $\mathrm{Re}_b = 150$ and $\mathrm{Re}_b = 34$. In Fig. 10 the jet forms at the end of a fast collapsing spherical cap by involution of the bubble wall. A high pressure region forms due to the in-rushing liquid. The magnitude of pressure, however, is several orders of magnitude smaller than after the self-impact of annular inflow in Fig. 4, above. The high pressure region connected to the broad jet in Fig. 11 is one further order of magnitude smaller.

Figure 12 gives the jet speeds for all four series of simulations. For $\mathrm{Re}_b \lesssim 300$ jets are formed by involution of the upper bubble wall, as shown in Fig. 9 in the last three rows and in Figs 10 and 11. Data points of all series of simulations collapse on a single line. For $\mathrm{Re}_b \gtrsim 300$ fast jet formation is observed. Within a series of simulations, the jet speed seems to be roughly independent of Re_b, but differs between the series. We note, however, that the jet speed in the axially symmetric simulations numerically depends on the grid spacing, since jet formation arises from liquid self-impact at the axis, which is a nearly singular phenomenon. Nevertheless, we include these values here, since a trend in variation of the jet speed might be inferred from them.

Figure 13 shows the equivalent radius of the bubble, which is a measure of bubble size, at the moment of jet formation, $\mathcal{R}^{\mathrm{eq}}_{\mathrm{jf}}$. For fast jet formation and the jets forming after the collapse of a spherical cap, the moment of jet formation can be defined by a pressure maximum at the axis. Data concerning the formation of a slow jet, as shown in Fig. 9 (third row) are not included in Fig. 13, since this type of jet formation is not connected to a pressure maximum at the axis.

$\mathcal{R}^{\mathrm{eq}}_{\mathrm{jf}}$ is maximum at $\mathrm{Re}_b \simeq 100$ and decreases for smaller and larger Re_b. The transition from jet formation after the collapse of a spherical cap to jet formation after self-impact of an annular inflow is smooth in the quantity $\mathcal{R}^{\mathrm{eq}}_{\mathrm{jf}}$. Increasing Re_b further, fast jet formation happens later and later in the bubble evolution.

4. CONCLUSION

The dynamics of bubbles expanding and collapsing right at a solid boundary has been investigated numerically for a range of bubble sizes and liquid viscosities.

We find the formation of a fast, thin jet after self-impact from an annular inflow for a wide range of combinations of bubble size and liquid viscosity. In terms of a bubble Reynolds number, Re_b, as defined here, fast jet formation is found for $\mathrm{Re}_b \gtrsim 300$. For larger values of Re_b the formation of the fast jet happens later and later in the bubble evolution, whereas the average jet speed seems to be roughly independ-

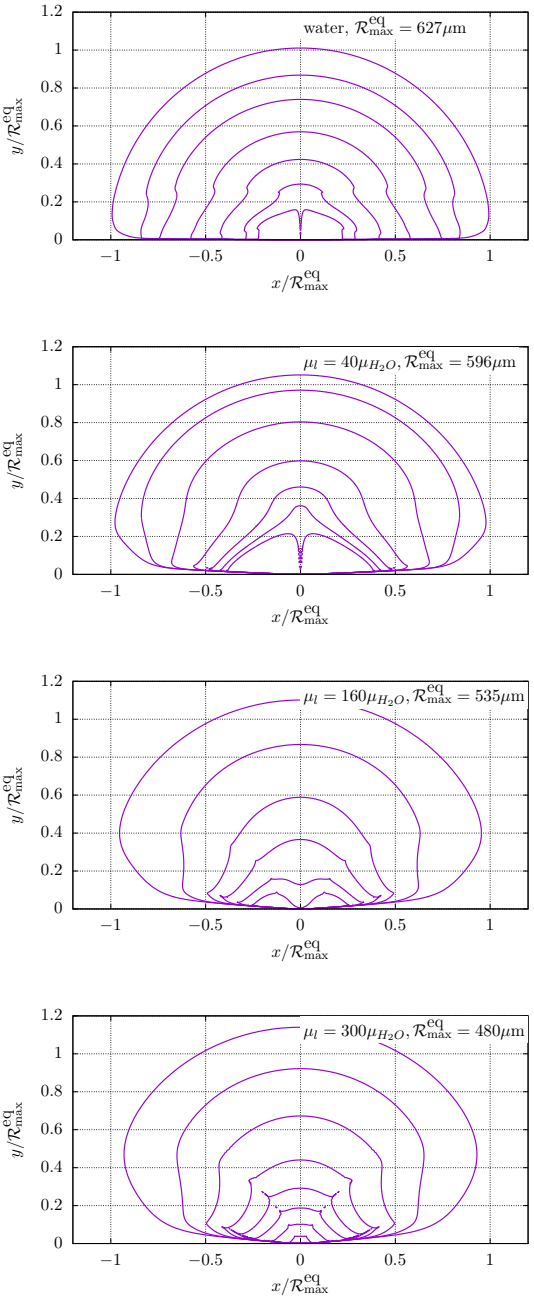

Figure 9. Bubble shape during the collapse phase for four liquids with viscosities $\mu_l = \mu_{H_2O}$ (reference bubble), $\mu_l = 40\mu_{H_2O}$, $\mu_l = 160\mu_{H_2O}$, and $\mu_l = 300\mu_{H_2O}$. The bubble Reynolds numbers are $\mathrm{Re}_b = 6289, 150, 34, 16$. Time proceeds from outer to inner curves.

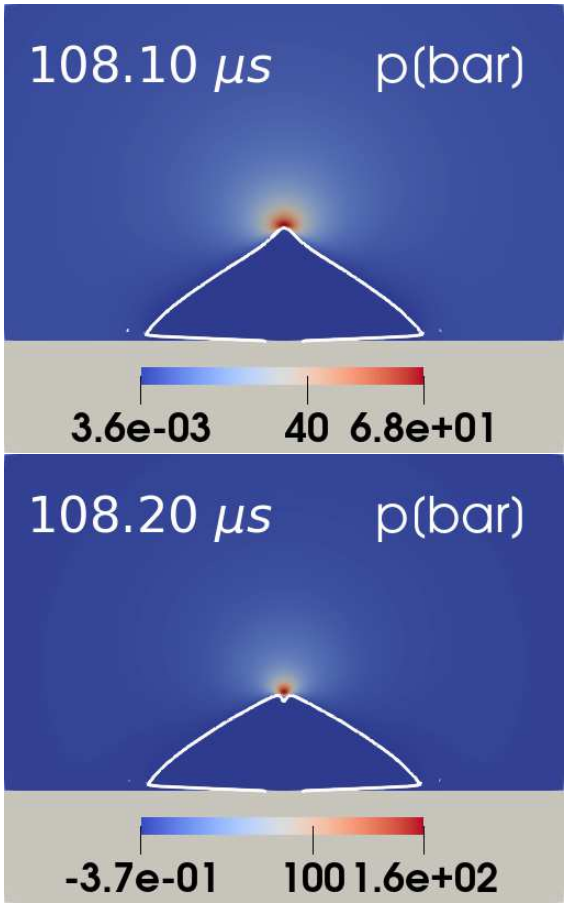

Figure 10. Bubble shape and pressure field in *bar* around jet formation for a bubble with $\mathrm{Re}_b = 150$, as in Fig. 9, second row.

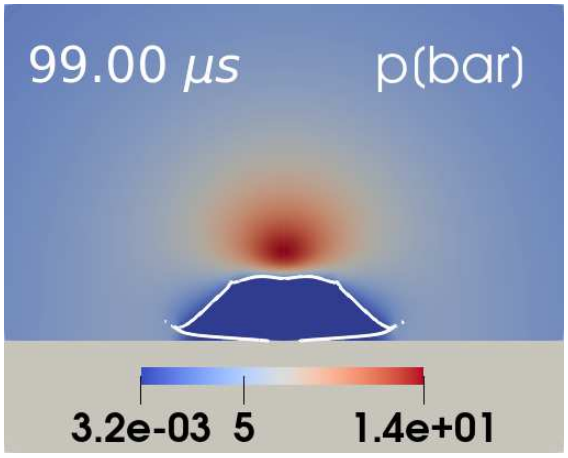

Figure 11. Bubble shape and pressure field in *bar* around jet formation for a bubble with $\mathrm{Re}_b = 34$, as in Fig. 9, third row.

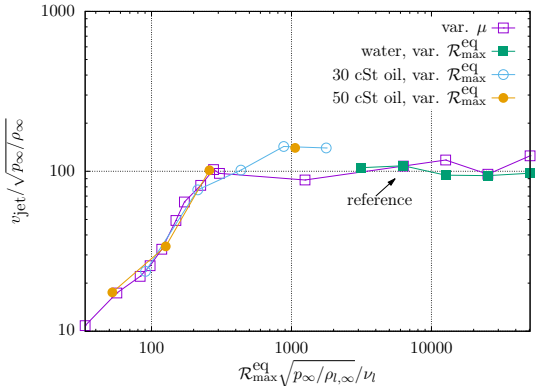

Figure 12. Normalized jet speed as a function of bubble Reynolds number.

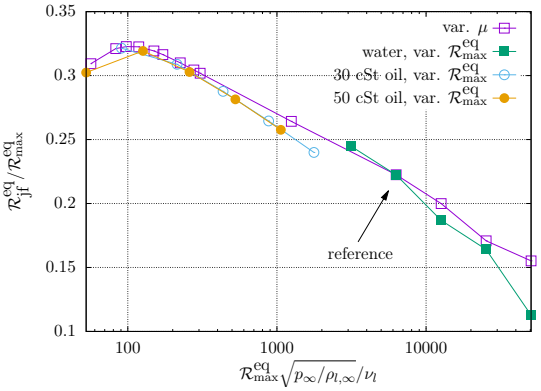

Figure 13. Equivalent radius of the bubble at the moment of jet formation.

ent of Re_b.

For $\mathrm{Re}_b \lesssim 300$ the jet formation mechanism changes and the jet forms by involution of the upper bubble wall. It has been demonstrated for $\mathrm{Re}_b = 150$ that the jet forms after a high curvature spherical cap has collapsed. For $\mathrm{Re}_b = 34$ a "slow", broad jet is formed. The transition between theses types of jet from involution of the bubble wall seems to be gradually. The jet speed continuously decreases with decreasing Re_b. For $\mathrm{Re}_b = 16$ no jet is found, the bubble stays simply connected during the first collapse and beyond.

ACKNOWLEDGMENTS

The work was supported in part by the Austrian Science Fund (FWF) (Grant No. I 5349-N) and the German Science Foundation (DFG) under contracts ME 1645/8-1, ME 1645/8-3 and ME 1645/5-2.

REFERENCES

[1] Philipp, A., and Lauterborn, W., 1998, "Cavitation erosion by single laser-produced bubbles", *J Fluid Mech*, Vol. 361, pp. 75–116.

[2] Brujan, E.-A., Nahen, K., Schmidt, P., and Vogel, A., 2001, "Dynamics of laser-induced cavitation bubbles near elastic boundaries: in-

fluence of the elastic modulus", *J Fluid Mech*, Vol. 433, pp. 283–314.

[3] Supponen, O., Obreschkow, D., Tinguely, M., Kobel, P., Dorsaz, N., and Farhat, M., 2016, "Scaling laws for jets of single cavitation bubbles", *J Fluid Mech*, Vol. 802, pp. 263–293.

[4] Lechner, C., Lauterborn, W., Koch, M., and Mettin, R., 2020, "Jet formation from bubbles near a solid boundary in a compressible liquid: Numerical study of distance dependence", *Phys Rev Fluids*, Vol. 5 (9), p. 093604.

[5] Koch, M., Rosselló, J. M., Lechner, C., Lauterborn, W., and Mettin, R., 2022, "Dynamics of a Laser-Induced Bubble above the Flat Top of a Solid Cylinder—Mushroom-Shaped Bubbles and the Fast Jet", *Fluids*, Vol. 7 (1), p. 2.

[6] Lechner, C., Lauterborn, W., Koch, M., and Mettin, R., 2019, "Fast, thin jets from bubbles expanding and collapsing in extreme vicinity to a solid boundary: A numerical study", *Phys Rev Fluids*, Vol. 4, p. 021601.

[7] Pishchalnikov, Y. A., Behnke-Parks, W. M., Schmidmayer, K., Maeda, K., Colonius, T., Kenny, T. W., and Laser, D. J., 2019, "High-speed video microscopy and numerical modeling of bubble dynamics near a surface of urinary stone", *J Acoust Soc Am*, Vol. 146, pp. 516 – 531.

[8] Koch, M., 2020, "Laser cavitation bubbles at objects: Merging numerical and experimental methods", PhD thesis, Georg-August-Universität Göttingen, Third Physical Institute, http://hdl.handle.net/21.11130/00-1735-0000-0005-1516-B.

[9] Koch, M., Rosselló, J. M., Lechner, C., Lauterborn, W., Eisener, J., and Mettin, R., 2021, "Theory-assisted optical ray tracing to extract cavitation-bubble shapes from experiment", *Exp Fluids*, Vol. 62 (3), p. 60.

[10] Reuter, F., and Ohl, C.-D., 2021, "Supersonic needle-jet generation with single cavitation bubbles", *Appl Phys Letters*, Vol. 118 (13), p. 134103.

[11] Benjamin, T. B., and Ellis, A. T., 1966, "The Collapse of Cavitation Bubbles and the Pressures thereby Produced against Solid Boundaries", *Philos Trans R Soc London, Ser A*, Vol. 260, pp. 221–240.

[12] Gonzalez Avila, S. R., Song, C., and Ohl, C.-D., 2015, "Fast transient microjets induced by hemispherical cavitation bubbles", *J Fluid Mech*, Vol. 767, pp. 31–51.

[13] Hupfeld, T., Laurens, G., Merabia, S., Barcikowski, S., Gökce, B., and Amans, D., 2020, "Dynamics of laser-induced cavitation bubbles at a solid–liquid interface in high viscosity and high capillary number regimes", *J Appl Phys*, Vol. 127 (4), p. 044306.

[14] Tryggvason, G., Brunner, B., Esmaeeli, A., Juric, D., Al-Rawahi, N., Tauber, W., Han, J., Nas, S., and Jan, Y.-J., 2001, "A Front-Tracking Method for the Computations of Multiphase Flow", *J Comput Phys*, Vol. 169, pp. 708–759.

[15] Weller, H. G., Tabor, G., Jasak, H., and Fureby, C., 1998, "A tensorial approach to computational continuum mechanics using object-oriented techniques", *Comput Phys*, Vol. 12 (6), pp. 620–631.

[16] Gschaider, B., Nilsson, H., Rusche, H., Jasak, H., Beaudoin, M., and Skuric, V., 2017, "The foam-extend project", URL `https://sourceforge.net/projects/foam-extend/`.

[17] Koch, M., Lechner, C., Reuter, F., Köhler, K., Mettin, R., and Lauterborn, W., 2016, "Numerical modeling of laser generated cavitation bubbles with the finite volume and volume of fluid method, using OpenFOAM", *Comput Fluids*, Vol. 126, pp. 71–90.